frontiers | Frontiers in Physics

TYPE Brief Research Report
PUBLISHED 26 September 2024
DOI 10.3389/fphy.2024.1474797

OPEN ACCESS

EDITED BY
Jian Dong,
Central South University, China

REVIEWED BY
Chengwang Xiao,
Central South University, China
Hailiang Lu,
Wuhan University, China

*CORRESPONDENCE
Junren Sun,
✉ sunjunren@cumtb.edu.cn

RECEIVED 02 August 2024
ACCEPTED 04 September 2024
PUBLISHED 26 September 2024

CITATION
Tang F, Zhang S, Zhu B and Sun J (2024) Outdoor large-scene 3D point cloud reconstruction based on transformer.
Front. Phys. 12:1474797.
doi: 10.3389/fphy.2024.1474797

Outdoor large-scene 3D point cloud reconstruction based on transformer

Fangzhou Tang[1], Shuting Zhang[1], Bocheng Zhu[1] and Junren Sun[1,2]*

[1]School of Electronics, Peking University, Beijing, China, [2]School of Artificial Intelligence, China University of Mining and Technology-Beijing, Beijing, China

3D point clouds collected by low-channel light detection and ranging (LiDAR) are relatively sparse compared to high-channel LiDAR, which is considered costly. To address this, an outdoor large-scene point cloud reconstruction (LSPCR) technique based on transformer is proposed in this study. The LSPCR approach first projects the original sparse 3D point cloud onto a 2D range image; then, it enhances the resolution in the vertical direction of the 2D range image before converting the high-resolution range image back to a 3D point cloud as the final reconstructed point cloud data. Experiments were performed on the real-world KITTI dataset, and the results show that LSPCR achieves an average accuracy improvement of over 60% compared to non-deep-learning algorithms; it also achieves better performance compared to the latest deep-learning algorithms. Therefore, LSPCR is an effective solution for sparse point cloud reconstruction and addresses the challenges associated with high-resolution LiDAR point clouds.

KEYWORDS

LiDAR, point cloud, transformer, reconstruction, autonomous driving

1 Introduction

Light detection and ranging (LiDAR) entails sensing the environment by emitting pulsed laser beams and receiving the reflected beams using echo detection equipment. The point cloud data obtained thus can provide information on spatial coordinates, shapes, and contours [1]. Given its high measurement accuracy and real-time response speed, LiDAR is widely used in high-precision applications such as autonomous driving and simultaneous localization and mapping (SLAM) [2]. However, the raw 3D point cloud data collected by most low-channel LiDAR are often sparse with high levels of noise and structural differences, whereas high-resolution LiDAR hardware involve significant costs. Therefore, reconstructing high-resolution point clouds from low-resolution point clouds has substantial value in engineering applications [3].

Outdoor large scenes often feature complex 3D point cloud structures, and these point cloud data are characterized by disorder, permutation invariance, and sparsity [4]. Unlike the adjacency relationships present in 2D images, point clouds are discrete and lack spatial continuity among the 3D points, making it impossible to directly apply existing deep-learning methods for point cloud enhancement or reconstruction [5]. Thus, 3D point cloud data must be converted to 2D images, such that 2D deep-learning networks can be used to achieve super-resolution. Range images differ significantly from optical images in terms of the pixel value representations, resolutions, and feature extraction directions [6]. Range image pixels represent depth information and typically have a lower resolution, whereas optical image pixels represent the intensities of red, green, and blue colors as well as have a higher resolution. These differences necessitate unique designs for point cloud super-resolution [7].

Currently, the methods available for reconstructing low-resolution point clouds can be categorized into traditional and deep-learning approaches. Among the traditional methods, interpolation algorithms (such as bilinear interpolation [8] and cubic interpolation [9]) are fast but are prone to overfitting problems in regions with significant curvature changes [10]. Subsequent methods based on Voronoi diagrams [11], locally optimal projections (LOPs) [12], and edge-aware point cloud enhancement [13] have been shown to be effective but require strong assumptions or manual parameter selection, making them unsuitable for most practical applications.

Deep-learning methods are shown to have significant advantages for predictions [14,15] as they do not require manual feature design and can implicitly describe the characteristics of images with different resolutions. Early research efforts on point cloud upsampling were mostly based on convolutional neural network (CNN) architectures, such as SR-ResNet [16], PU-Net [17], ILN [18], and self-supervised learning methods [19,20,21]. These methods primarily use encoder networks with convolutional and deconvolutional layers but are prone to edge-smoothing issues owing to regularization effects when processing range images. Since the proposal of ViT, transformer models have been used to achieve breakthroughs in computer vision applications [22]. The Swin transformer alleviates the computational burden of self-attention by partitioning images [23,24]. Accordingly, numerous works were proposed, such as the height-aware lidar super-resolution (HALS) framework [25], PU-transformer [26], Swin-T-NFC conditional random fields [27], and PU-Dense [28], which have significantly enhanced point cloud reconstruction performances through multihead self-attention structures, position fusion blocks, and sliced Wasserstein distance techniques.

The present work proposes a point cloud reconstruction method specifically designed for LiDAR range images, named large-scene point cloud reconstruction (LSPCR). This method utilizes a U-shaped network structure similar to that of U-Net and skip connections as in ResNet to connect the encoder and decoder parts. Given a low-resolution range image and its features on the vertical information distribution, we used row patches instead of square patches to tokenize the range image. Additionally, by drawing inspiration from the Swin transformer design, we introduced cross-shaped window self-attention (CSwin) to design the core components for LSPCR. CSwin computes the self-attention in cross-shaped windows formed by horizontal and vertical stripes, making it suitable for vertical-direction super-resolution tasks of range images. Experiments were conducted with the KITTI dataset, and the results demonstrate that LSPCR offers the latest advancements for outdoor data.

2 Methods

2.1 Problem statement

Each point p_i in a LiDAR system is represented using the three-dimensional coordinates (x_i, y_i, z_i). A LiDAR point cloud in a single frame comprises multiple p_i, denoted as $P = \{p_1, \ldots, p_n\}$, where n is the total number of points equal to the product of the vertical resolution H and horizontal resolution W. Our objective here is to reconstruct a high-resolution point cloud P_h from a low-resolution point cloud P_l, such that the number of points in the high-resolution point cloud is $n_h = \lambda \times n_l$, where λ represents the difference in the number of LiDAR beams. Although P_l and P_h share the same field of view (FoV), P_h has a higher resolution in the vertical direction. Therefore, given $n_h = H_h \times W_h$ and $n_l = H_l \times W_l$, it follows that $H_h = \lambda \times H_l$ and $W_h = W_l$. In the reconstruction process, we follow the standard method of converting LiDAR point clouds into range images, as illustrated in Equation 1.

$$\begin{pmatrix} u \\ v \end{pmatrix} = \begin{pmatrix} \frac{W}{2} - \frac{W}{2\pi}\arctan\left(\frac{y}{x}\right) \\ \frac{H}{\Lambda_{\max} - \Lambda_{\min}}\left(\Lambda_{\max} - \arctan\left(\frac{z}{\sqrt{x^2 + y^2}}\right)\right) \end{pmatrix}. \tag{1}$$

The coordinates u and v on the left side of the equation represent the row and column indices of the range image, while $\Lambda_{\max}$ and $\Lambda_{\min}$ denote the maximum and minimum vertical angles of the LiDAR's FoV, respectively. Through these steps, the point cloud reconstruction problem is transformed into a super-resolution problem for 2D images. Specifically, it involves forecasting a high-resolution range image $I_h \in \mathbb{R}^{1\times H_h\times W}$ using a low-resolution range image $I_l \in \mathbb{R}^{1\times H_l\times W}$. Subsequently, by combining I_h with the inverse of Equation 1, we can compute the high-resolution point cloud P_h.

2.2 Network structure overview

The LSPCR method employs a U-shaped network architecture and integrates information from the encoder and decoder modules through skip connections, as shown in Figure 1. The network is composed of multiple CSwin blocks with different parameters. Initially, LSPCR concatenates the input and maps it to a high-dimensional feature space. To accommodate the fact that the width of the range image is much larger than its height, we adopt a row-based patching approach in the tokenization phase using a 1 × 4 dimension for the range image, which has the advantage of compressing the horizontal information while retaining the vertical information as is. This aligns with our goal of preserving and extending the vertical information in the range image.

The encoder is designed to generate feature maps through a series of stages, each of which includes a CSwin transformer block and a patch merging layer. This configuration reduces the resolution by a factor of 4 while increasing the dimensionality by a factor of 2. At each stage, multiple CSwin instances are executed locally in parallel while being interspersed with two multilayer perceptron layers and residual connections from the input. The decoder, which is responsible for upsampling, operates in reverse to the encoder and is designed symmetrically. Initially, the dimensionality of the feature map is reduced by a factor of 2 and the resolution is expanded; here, skip connections are employed to retain the existing geometric information. At the final stage, a single-channel range image with high resolution is obtained. The final part of the network includes a 1 × 1 convolutional layer followed by a leaky rectified linear unit (ReLU) activation layer and a pixel shuffle layer. Then, another 1 × 1 convolutional layer is used to obtain the final projection. The pixelwise $L1$ loss is used as the loss function for training the LSPCR model.

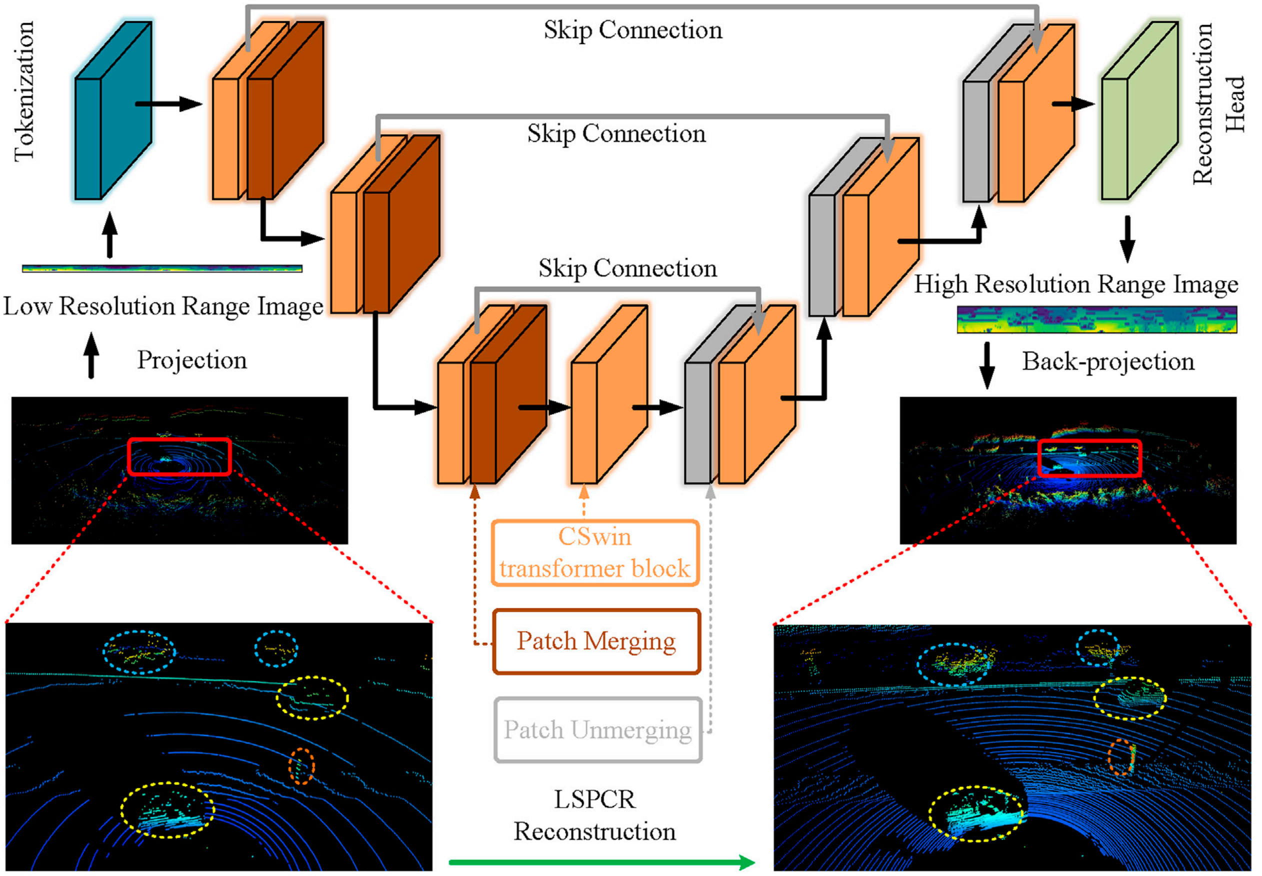

FIGURE 1
Network architecture details of the proposed LSPCR method employing symmetric designs for the encoder and decoder. The basic unit of the encoder consists of two CSwin transformer blocks and a patch merging layer to reduce the spatial resolution of the feature map. The basic unit of the decoder includes a patch splitting layer and two subsequent blocks to restore the resolution. The image sizes are 16 × 256 × 96, 8 × 128 × 192, 4 × 64 × 384, 2 × 32 × 768 corresponding to height × width × number of channels. Additionally, for better data adaptability, the range images are preprocessed with a logarithmic transformation before being input to the network. The figure shows the original sparse point cloud, low-resolution range image, high-resolution image, and reconstructed dense point cloud. The elliptical dashed lines directly highlight the details of the point cloud reconstruction.

2.2.1 CSwin transformer block

CSwin offers several advantages for processing range images, as depicted in Figure 2A. By calculating the self-attention in both horizontal and vertical directions, CSwin captures the local details and integrates the global information effectively. It is particularly well-suited for range images, which have unique geometric and depth characteristics, as it can extract features in the high-resolution vertical direction finely while maintaining the efficiency in the horizontal direction. CSwin accurately captures the edges of sharp objects while avoiding smoothing issues as well as preserving the fine structures and geometry. Its multiscale feature extraction capability allows handling different depths and distances to enhance the reconstruction accuracy and robustness of complex scenes.

This method involves initial partitioning of the input feature map into horizontal and vertical stripes of equal widths. These vertical and horizontal stripes form cross-shaped windows, from which the self-attention is computed. The computations within these stripes are performed in parallel. Initially, the input features $X \in \mathbb{R}^{(H \times W) \times C}$ are linearly projected onto K heads in the CSwin self-attention mechanism. Local self-attention is then calculated for each head within the horizontal or vertical stripes. The input features X are divided into M non-overlapping horizontal stripes $[X_1, X_2, \ldots, X_M]$ of equal widths sw for horizontal self-attention, where each stripe contains $sw \times W$ tokens. The queries, keys, and values for the k-th head are denoted as $Q_k, K_k, andV_k$, respectively, with d_k dimensions. The output of the self-attention for the horizontal stripes for the k-th head is given by Equations 2, 3 as follows:

$$Y_k^i = \text{Attention}\left(X_i W_k^Q, X_i W_k^K, X_i W_k^V\right) \tag{2}$$

$$\text{H} - \text{Attention}_k(X) = \left[Y_k^1, Y_k^2, \ldots, Y_k^M\right] \tag{3}$$

where $X_i \in \mathbb{R}^{(sw \times W) \times C}$, $M = \frac{H}{sw}$, and $W_k^Q, W_k^K, W_k^V \in \mathbb{R}^{C \times d_k}$. The process of self-attention calculation for the vertical stripes is similar to that for the horizontal stripes. The output for the k-th head is denoted as $\text{V} - \text{Attention}_k(X)$. The stripe width sw is a crucial parameter in CSwin. Based on the depth of the network, smaller widths may be used for the shallow layers, while larger widths are applied to the deeper layers.

We also use the relative positional encoding (RPE) method, which enhances positional encoding by incorporating relative positional

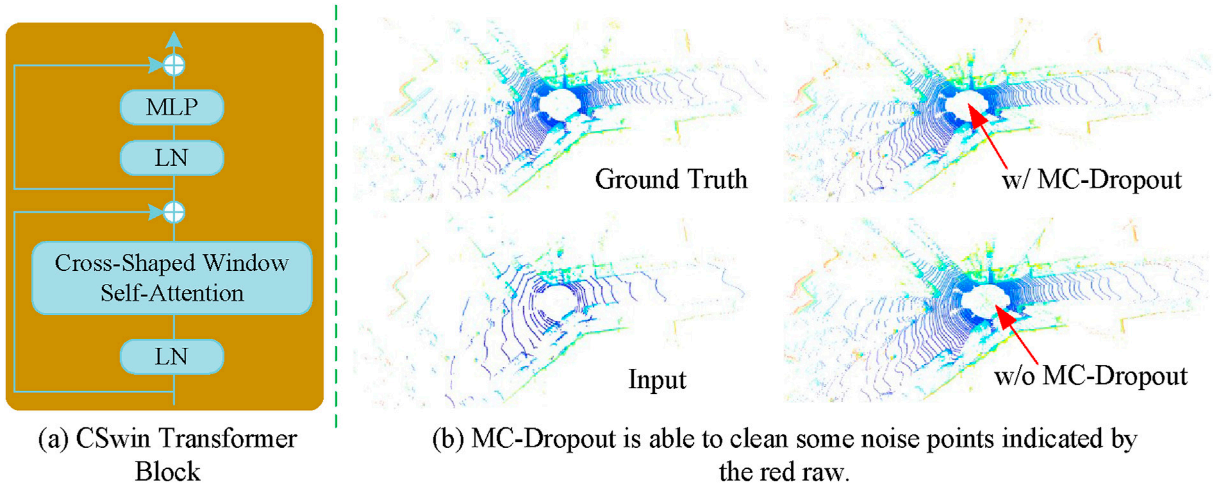

(a) CSwin Transformer Block

(b) MC-Dropout is able to clean some noise points indicated by the red raw.

FIGURE 2
(A) CSwin transformer block and **(B)** Monte Carlo dropout performance.

information directly in the self-attention calculation. RPE captures the spatial structure and relative positional relationships among image data, which are crucial for visual tasks. The method entails application of a relative position bias to the attention mechanism to improve the model's ability to generalize to images of different sizes and resolutions. Given the input features $X \in \mathbb{R}^{(H\times W)\times C}$, let Q, K, and V be the linear projections for the queries, keys, and values, respectively. Then, $Q = XW^Q$, $K = XW^K$, and $V = XW^V$, where W^Q, W^K, and $W^V \in \mathbb{R}^{C\times d_k}$ are the linear transformation matrices for the queries, keys, and values, respectively. In the RPE method, a relative position bias matrix $\Gamma \in \mathbb{R}^{n\times n}$ is calculated, in which each element Γ_{ij} represents the relative position bias between positions i and j. The attention score matrix is given by $A = \frac{QK^T}{\sqrt{d_k}} + \Gamma$. The attention output is then computed by normalizing the score matrix with the softmax function as $\text{Attention}(Q, K, V) = \text{softmax}(A)V$. Specifically, the attention output is obtained by Equation 4.

$$Z = \text{softmax}\left(\frac{QK^T}{\sqrt{d_k}} + \Gamma\right)V \tag{4}$$

The relative position bias Γ_{ij} is typically computed using a learnable relative position bias vector r as $\Gamma_{ij} = r_{j-i}$. This means that the bias depends only on the relative position difference $j - i$ and effectively captures the relative position information when calculating attention weights.

2.2.2 Monte Carlo dropout

Monte Carlo (MC) dropout is an uncertainty estimation technique used to simulate different model parameters by retaining the dropout layers during the inference phase and performing the predictions T times. The model parameters follow a Bernoulli distribution, and the final prediction is obtained by averaging the T predictions [29]. Let f be the model output when given an input x with parameters θ. For the input x, T forward passes are performed with the dropout enabled each time as $\hat{y}_t = f(x, \theta_t)$, for $t = 1, \ldots, T$ ($T = 40$ in our work); here, θ_t represents the model parameters with dropout applied during the t-th forward pass. The final prediction result is the average of these outputs, as expressed in Equation 5.

$$\bar{y} = \frac{1}{T}\sum_{t=1}^{T}\hat{y}_t. \tag{5}$$

The uncertainty estimate can be obtained by calculating the variance or standard deviation of these prediction results as given by Equation 6.

$$\hat{\sigma}^2(\hat{y}) = \frac{1}{T}\sum_{t=1}^{T}(\hat{y}_t - \bar{y})^2. \tag{6}$$

For the LiDAR point clouds, we can interpret uncertainty as the noise in the estimation of the 3D coordinates. Therefore, by employing a predefined threshold parameter λ, the noisy points can be eliminated to acquire the final prediction $\bar{\dagger}$ based on the decision rule specified in Equation 7. This performance is shown in Figure 2B.

$$\bar{\dagger} = \begin{cases} \bar{y}, & if\,\bar{\sigma} < \lambda * \bar{y} \\ 0, & otherwise \end{cases} \tag{7}$$

3 Experiment

3.1 Setup details

Experiments were conducted on the real-world KITTI dataset to evaluate the performance of the proposed method. The data used for training and testing were generated by creating randomly positioned range images from raw LiDAR data. Here, 30,000 samples were selected for training, and 3,000 samples were used for testing. The 16-line LiDAR point cloud data were extracted uniformly from 64-line LiDAR point clouds to prevent spatial overlap as sequential images were not employed in this study. The experiments were conducted with the PyTorch framework on an NVIDIA GeForce RTX 4090 graphics processing unit. All experiments involved 4 × point cloud data augmentation (from 16-channels to 64-channels), a batch size of 16, and a default of 650 training epochs. AdamW was chosen as the optimization method with a learning rate of $5e - 4$ and weight decay factor of 0.01.

TABLE 1 Quantitative comparisons between state-of-the-art LiDAR and image super-resolution methods. Identical data splits were used for training and evaluation of all methods.

Model	MAE	IoU	CD
Bilinear	2.0892	0.1035	0.5934
Cubic	2.8580	0.0957	0.8307
Super-resolution neural operator (SRNO)	0.8350	0.1986	0.4368
Hybrid Attention Transformer (HAT)	0.6856	0.1992	0.2483
Image Restoration Using Swin Transformer (SWIN-IR)	1.2972	0.2685	0.7244
SR-ResNet	1.5493	0.2365	0.8032
Implicit LiDAR Network (ILN)	1.0528	0.3289	0.2756
Local Implicit Image Function (LIIF)	0.6143	0.3186	0.1891
Lidar Super-resolution (LIDAR-SR)	0.5674	0.1020	0.2141
LSPCR (Ours)	**0.4143**	**0.4133**	**0.1253**

TABLE 2 Computational complexity of the proposed LSPCR.

Model	Swin-IR	LiDAR-SR	ILN	LSPCR(Ours)
Number of parameters	11.8 M	34.6 M	1.3 M	33.1 M
Inference time	0.91 s	0.72 s	0.52 s	0.61 s

The mean absolute error (MAE) was evaluated for all pixels in a generated 2D range image using Equation 8. The performance was also assessed on the basis of the 3D points reconstructed by the neural network using the Chamfer distance (CD) to measure the Euclidean distance between two point clouds, as shown in Equation 9. Additionally, the point cloud was voxelized with a voxel size of $0.1m$. A given voxel was classified as occupied if it contained at least one point cloud. The intersection over union (IoU) was then computed based on the occupancy rate.

$$MAE = \frac{1}{n}\sum_{i=1}^{n}\left|y_i - \hat{y}_i\right| \tag{8}$$

where y_i is the i-th true value, $\hat{y}_i$ is the i th predicted value, and n is the number of samples.

$$d_{CD}(\Omega_1,\Omega_2) = \frac{1}{|\Omega_1|}\sum_{x\in\Omega_1}\min_{y\in\Omega_2}\|x-y\|_2^2 + \frac{1}{|\Omega_2|}\sum_{y\in\Omega_2}\min_{x\in\Omega_1}\|y-x\|_2^2 \tag{9}$$

where Ω_1 and Ω_2 are two point cloud sets; $|\Omega_1|$ and $|\Omega_2|$ are the numbers of points in Ω_1 and Ω_2, respectively; $\|x-y\|_2$ indicates the distance between the points x and y.

3.2 Experiments

3.2.1 Results

We selected nine state-of-the-art (SOTA) methods for comparison with the proposed approach, and the quantitative results of our experiments are presented in Table 1. It is noted that LSPCR achieves the best performance for all three metrics. Traditional interpolation methods perform worse than deep learning, which also indicates that the non-adjacency in point cloud data is difficult to model directly. In addition, it is worth noting that the MAE for the 2D image does not exactly correlate directly with the 3D metrics; for example, LIDAR-SR has better MAE results but performs worse in terms of the IoU and CD. This suggests that there are a large number of invalid noise points between real objects.

To evaluate the complexity of the models, we elaborated the model parameter numbers and inference times for single samples. Table 2 summarizes the specific values of the numbers of parameters for the different models and their inference times for a single sample. Swin-IR has fewer parameters as its decoding part is referenced to ResNet. LiDAR-SR's network design is more similar to that of LSPCR. ILN has the least number of parameters because of the learned interpolation weights. In addition, the inference speeds are as expected, with ILN demonstrating the fastest inference, LiDAR-SR and LSPCR showing similar inference speeds, and Swin-IR having the slowest inference.

3.2.2 Ablation studies

Table 3 shows the results of our ablation experiments. We observed the effects of CSwin by replacing the CSwin module with the ViT module and deleting the MC module. The table clearly shows the superior performance with the CSwin and MC modules, which is in line with our expectation. Compared to RGB

TABLE 3 Ablation study results.

Blocks	MC	MAE	IoU	CD
CSwin	×	0.4196	0.4095	0.1306
CSwin	✓	0.4143	0.4133	0.1253
ViT	×	1.4796	0.2796	0.2765
ViT	✓	1.4698	0.2895	0.2568

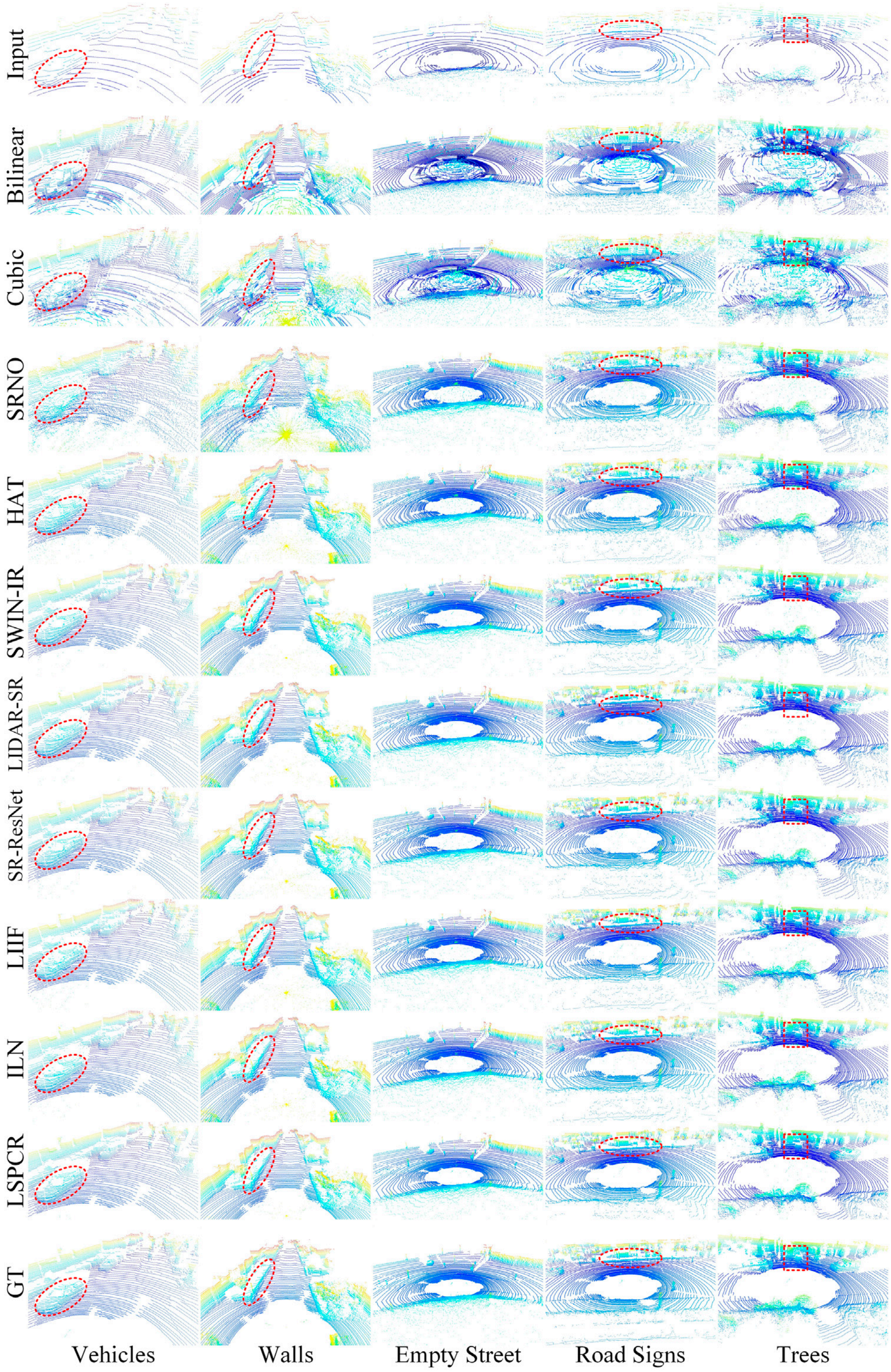

FIGURE 3
Detailed comparisons with images from the KITTI dataset demonstrate the performances of the LSPCR and state-of-the-art methods. Different types of point cloud details (vehicles, walls, empty street, road signs, and trees) were selected for comparison. The results show that the point clouds obtained through LSPCR are more accurate and have significantly fewer noise points.

datasets, LiDAR datasets usually have low volumes, and ViT lacks the ability to focus on local features; this weakens ViT's performance on LIDAR datasets. In addition, the use of MC dropout shows some improvements in all metrics, indicating its effectiveness.

3.3 Discussion

Figure 3 depicts the results of different methods. We selected five types of scenes (vehicles, walls, empty street, road signs, and

TABLE 4 Comparison results under different conditions.

Different conditions	MAE	IoU	CD
Vehicles	0.4139	0.4134	0.1252
Walls	0.4149	0.4136	0.1248
Empty street	0.4137	0.4138	0.1243
Road signs	0.4139	0.4140	0.1252
Trees	0.4141	0.4135	0.1256

trees) to demonstrate the performance of the LSPCR method. The red dashed lines show the details that we focus on. For instance, in the case of vehicles, LSPCR significantly restores a better profile, particularly around the A-pillar. It is clear in Figure 3 that the direct interpolation approach of traditional methods leads to large amounts of invalid noise, which are mitigated well by deep-learning methods owing to their implicit modeling capabilities; among the deep-learning methods, LSPCR achieves the best visual effects. Additionally, LSPCR clearly recovers the outline of the vehicle, details of the wall, shape of the road sign, and the tree. Meanwhile, the point cloud noise reconstructed by LSPCR is significantly less than those of other deep-learning methods, which is also consistent with the performance for the 3D evaluation metrics. We counted the point clouds with more distinct features and provide specific evaluation results in Table 4; the data in the table show that the LSPCR method produces stable reconstruction results under different conditions.

4 Conclusion

This work addresses the problem of enhancement of 3D point cloud data by transforming reconstruction into a super-resolution task for 2D range images. A novel LiDAR point cloud reconstruction method called LSPCR is proposed here, which converts 3D point clouds to 2D range images before upsampling them. LSPCR is designed on the basis of the Swin transformer by optimizing the patch partitioning and attention modules to better accommodate the features of range images. Experiments were performed with images from the real-world dataset KITTI, and the results demonstrate that LSPCR outperforms traditional interpolation methods while achieving better performance over extant deep-learning methods.

Data availability statement

The raw data supporting the conclusions of this article will be made available by the authors without undue reservation.

Author contributions

FT: writing–review and editing and writing–original draft. SZ: writing–review and editing, software, investigation, and conceptualization. BZ: writing–review and editing and supervision. JS: writing–review and editing, resources, methodology, and funding acquisition.

Funding

The authors declare that financial support was received for the research, authorship, and/or publication of this article. This work was supported in part by the Basic Science Center Program of the National Natural Science Foundation of China (no. 62388101) and the Fundamental Research Funds for the Central Universities" (2023ZKPYJD06).

Acknowledgments

The authors would like to thank the editors and reviewers for their efforts in supporting the publication of this paper.

Conflict of interest

The authors declare that the research was conducted in the absence of any commercial or financial relationships that could be construed as a potential conflict of interest.

Publisher's note

All claims expressed in this article are solely those of the authors and do not necessarily represent those of their affiliated organizations or those of the publisher, editors, and reviewers. Any product that may be evaluated in this article or claim that may be made by its manufacturer is not guaranteed or endorsed by the publisher.

References

1. Dinesh C, Cheung G, Bajić IV. 3D point cloud super-resolution via graph total variation on surface normals. In: 2019 IEEE international conference on image processing (ICIP); 22-25 September 2019; Taipei, Taiwan: IEEE (2019). 4390–4. doi:10.1109/ICIP.2019.8803560

2. Triess LT, Peter D, Rist CB, Enzweiler M, Zöllner JM. Cnn-based synthesis of realistic high-resolution lidar data. In: 2019 IEEE intelligent vehicles symposium (IV). IEEE Press (2019). p. 1512–9. doi:10.1109/IVS.2019.8813771

3. Ye S, Chen D, Han S, Wan Z, Liao J. Meta-pu: an arbitrary-scale upsampling network for point cloud. *IEEE Trans Visualization Computer Graphics* (2021) 28: 3206–18. doi:10.1109/tvcg.2021.3058311

4. Savkin A, Wang Y, Wirkert S, Navab N, Tombari F. Lidar upsampling with sliced wasserstein distance. *IEEE Robotics Automation Lett* (2023) 8:392–9. doi:10.1109/LRA.2022.3214791

5. Chen T-Y, Hsiao C-C, Huang C-C. Density-imbalance-eased lidar point cloud upsampling via feature consistency learning. *IEEE Trans Intell Vehicles* (2023) 8: 2875–87. doi:10.1109/TIV.2022.3162672

6. Sinha A, Bai J, Ramani K. Deep learning 3d shape surfaces using geometry images. In: European conference on computer vision; October 11-14, 2016: Amsterdam, Netherlands: Springer (2016).

7. Su H, Maji S, Kalogerakis E, Learned-Miller E. Multi-view convolutional neural networks for 3d shape recognition. In: Proceedings of the 2015 IEEE international Conference on computer vision (ICCV); (United States: IEEE computer society) (2015). 945–53. doi:10.1109/ICCV.2015.114

8. Mastyło M. Bilinear interpolation theorems and applications. *J Funct Anal* (2013) 265:185–207. doi:10.1016/j.jfa.2013.05.001

9. Keys R. Cubic convolution interpolation for digital image processing. *IEEE Trans Acoust Speech, Signal Process* (1981) 29:1153–60. doi:10.1109/TASSP.1981.1163711

10. Tang F, Gui L, Liu J, Chen K, Lang L, Cheng Y. Metal target detection method using passive millimeter-wave polarimetric imagery. *Opt Express* (2020) 28:13336–51. doi:10.1364/OE.390385

11. Alexa M, Behr J, Cohen-Or D, Fleishman S, Levin D, Silva C. Computing and rendering point set surfaces. *IEEE Trans Visualization Computer Graphics* (2003) 9: 3–15. doi:10.1109/TVCG.2003.1175093

12. Lipman Y, Cohen-Or D, Levin D, Tal-Ezer H. Parameterization-free projection for geometry reconstruction. In: *ACM SIGGRAPH 2007 papers*. New York, NY, USA: Association for Computing Machinery (2007). p. 22–es. doi:10.1145/1275808.1276405

13. Huang H, Li D, Zhang H, Ascher U, Cohen-Or D. Consolidation of unorganized point clouds for surface reconstruction. *ACM Trans Graph* (2009) 28:1–7. doi:10.1145/1618452.1618522

14. Wang Y, Yu A, Cheng Y, Qi J. Matrix diffractive deep neural networks merging polarization into meta devices. *Laser & Photon Rev* (2023b) 18:2300903. doi:10.1002/lpor.202300903

15. Cheng Y, Tian X, Zhu D, Wu L, Zhang L, Qi J, et al. Regional-based object detection using polarization and Fisher vectors in passive millimeter-wave imaging. *IEEE Trans Microwave Theor Tech* (2023) 71:2702–13. doi:10.1109/TMTT.2022.3230940

16. Ledig C, Theis L, Huszar F, Caballero J, Cunningham A, Acosta A, et al. (2017). Photo-realistic single image super-resolution using a generative adversarial network. In: 2017 IEEE Conference on Computer Vision and Pattern Recognition CVPR; 21-26 July 2017; Honolulu, United States: IEEE.

17. Yu L, Li X, Fu C-W, Cohen-Or D, Heng P-A. Pu-net: point cloud upsampling network. In: 2018 IEEE/CVF conference on computer vision and pattern recognition; 18-23 June 2018; Salt Lake City, UT, USA: IEEE (2018). p. 2790–9. doi:10.1109/CVPR.2018.00295

18. Kwon Y, Sung M, Yoon S. Implicit lidar network: lidar super-resolution via interpolation weight prediction. In: 2022 international conference on robotics and automation (ICRA); 23-27 May 2022; Philadelphia, PA, USA: IEEE Press (2022). p. 8424–30. doi:10.1109/ICRA46639.2022.9811992

19. Zhao W, Liu X, Zhai D, Jiang J, Ji X. Self-supervised arbitrary-scale implicit point clouds upsampling. *IEEE Trans Pattern Anal Machine Intelligence* (2023) 45: 12394–407. doi:10.1109/TPAMI.2023.3287628

20. Zhao Y, Hui L, Xie J. Sspu-net: self-supervised point cloud upsampling via differentiable rendering. In: Proceedings of the 29th ACM international conference on multimedia. New York, NY, USA: Association for Computing Machinery (2021). p. 2214–23. doi:10.1145/3474085.3475381

21. Ma F, Cavalheiro GV, Karaman S. Self-supervised sparse-to-dense: self-supervised depth completion from lidar and monocular camera. In: 2019 international conference on robotics and automation (ICRA); 20-24 May 2019; Montreal, QC, Canada: IEEE Press (2019). p. 3288–95. doi:10.1109/ICRA.2019.8793637

22. Dosovitskiy A, Beyer L, Kolesnikov A, Weissenborn D, Zhai X, Unterthiner T, et al. (2020). An image is worth 16x16 words: transformers for image recognition at scale. *ArXiv* abs/2010.11929

23. Liu Z, Lin Y, Cao Y, Hu H, Wei Y, Zhang Z, et al. Swin transformer: hierarchical vision transformer using shifted windows. In: 2021 IEEE/CVF international conference on computer vision (ICCV); 10-17 October 2021; Montreal, QC, Canada: IEEE (2021). p. 9992–10002. doi:10.1109/ICCV48922.2021.00986

24. Dong X, Bao J, Chen D, Zhang W, Yu N, Yuan L, et al. Cswin transformer: a general vision transformer backbone with cross-shaped windows. In: 2022 IEEE/CVF conference on computer vision and pattern recognition CVPR; 18-24 June 2022; New Orleans, United States: IEEE (2021). p. 12114–24.

25. Eskandar G, Sudarsan S, Guirguis K, Palaniswamy J, Somashekar B, Yang B (2022). Hals: a height-aware lidar super-resolution framework for autonomous driving. arxiv.org/abs/2202.03901.

26. Qiu S, Anwar S, Barnes N. Pu-transformer: point cloud upsampling transformer. In: Wang L, Gall J, Chin T-J, Sato I, Chellappa R, editors. *Computer vision – ACCV 2022*. Cham: Springer Nature Switzerland (2023). p. 326–43.

27. Wang S, Wang H, She S, Zhang Y, Qiu Q, Xiao Z. Swin-t-nfc crfs: an encoder–decoder neural model for high-precision uav positioning via point cloud super resolution and image semantic segmentation. *Comput Commun* (2023a) 197: 52–60. doi:10.1016/j.comcom.2022.10.011

28. Akhtar A, Li Z, Auwera GVd., Li L, Chen J. Pu-dense: sparse tensor-based point cloud geometry upsampling. *IEEE Trans Image Process* (2022) 31:4133–48. doi:10.1109/TIP.2022.3180904

29. [Dataset] Gal Y, Ghahramani Z (2016) Dropout as a bayesian approximation: representing model uncertainty in deep learning. arxiv.org/abs/1506.02142.